International Journal of Plasticity 91 (2017) 300–317

Contents lists available at ScienceDirect

International Journal of Plasticity

journal homepage: www.elsevier.com/locate/ijplas

A viscoelastic constitutive model for shape memory polymers based on multiplicative decompositions of the deformation gradient

Yunxin Li, Yuhao He, Zishun Liu*

International Center for Applied Mechanics, State Key Laboratory for Strength and Vibration of Mechanical Structures, Xi'an Jiaotong University, Xi'an, 710049, People's Republic of China

ARTICLE INFO

Article history:
Received 27 November 2016
Received in revised form 29 March 2017
Accepted 5 April 2017
Available online 7 April 2017

Keywords:
Constitutive model
Large strain
Phase transition
Shape memory polymers
Viscoelastic

ABSTRACT

Shape memory polymers (SMPs) are a class of polymeric smart materials that have the capacity to return from a deformed state (impermanent shape) to their original state (permanent shape) by temperature stimulus. In this work, we propose a novel phase-transition-based viscoelastic model including the time factor for shape memory polymers (SMPs), which has a clearer physical significance. To describe the phase transition phenomenon of SMPs, our new model defines different constitutive structures for above and below transformation temperature separately. As the proposed viscoelastic model is based on multiplicative thermoviscoelasticity, it can not only be used for different types of SMP materials, but also can be used to treat large strain problems. To validate the model's availability and show the model's capability of reproducing the shape memory effect (SME), two testing examples are predicted with this new constitutive model. The prediction results of the simulation are in good agreement with the available experimental results.

1. Introduction

Shape memory polymers (SMPs) are a kind of soft and smart materials that can maintain a deformed state (impermanent shape) with a pre-deformation at a high temperature and subsequently cooling it down to a lower temperature. The memorized original state (permanent shape) can be recovered by rising the temperature. Compared with traditional shape memory materials *e.g.*, shape memory alloys (SMAs) (Ashrafi et al., 2016; Oliveira et al., 2014; Poorasadion et al., 2015; Yu et al., 2014), SMPs have many advantages in engineering applications, including highly flexible programming, tunable properties, biodegradability, biocompatibility, light weight and low cost (Baghani et al., 2012; Hager et al., 2015; Leng et al., 2009). Due to the superior performance of this kind of materials, SMPs have been widely used in artificial muscles (Marshall et al., 2014; Ohm et al., 2010), Shaping tissue (Huang et al., 2013), functional textiles (Castano and Flatau, 2014; Hu and Chen, 2010), switchable/recoverable optics (Lee et al., 2014; Xu et al., 2013), self-healing materials (Li et al., 2012; Li and Shojaei, 2012; Shojaei and Li, 2014; Voyiadjis et al., 2011a, b), active aircraft equipment, aerospace structures (Behl et al., 2010; Hu et al., 2012) and pattern transformation (He et al., 2015; Liu et al., 2015). With the increasing significant progress and

---

* Corresponding author.
E-mail address: zishunliu@mail.xjtu.edu.cn (Z. Liu).

http://dx.doi.org/10.1016/j.ijplas.2017.04.004
0749-6419/

deeper understanding of SMPs, they are holding a great importance in both academics and industrial fields, which is further promoting the fundamental study of these types of materials. Compared with other depth-researched polymers (*e.g.,* Nylon (Farrokh and Khan, 2010), gels (Chester and Anand, 2010, 2011; Chester et al., 2015), Nitrile Butadiene Rubber (Khan et al., 2010)), the thermomechanical mechanisms of SMPs are still not very clear. Therefore, it is imperative to develop more suitable constitutive models for benefiting the exploitation of new-type SMPs and extending the understanding of the complex thermomechanical mechanisms.

Generally, to develop new macro-constitutive models, two approaches have been mainly adopted for SMPs: viscoelastic modeling and phase transition modeling. Viscoelastic modeling approach applies rheological models with time-dependent and temperature-dependent property parameters (Hu et al., 2012). Thermoviscoelastic models commonly consist of spring elements, dashpot elements and frictional elements. The viscosity, an important feature of polymers, has been introduced into these viscoelastic models. Thus, the models can not only describe the SME of SMPs qualitatively, but also characterize viscoelastic properties and the rate-dependent behaviors. Early use of the viscoelastic modeling approach was recommended by Tobushi et al. (1997, 2001). Such simple models have recently been inherited and developed. Nguyen et al. (2008) established a new approach to modeling amorphous SMPs with the assumption that structural and stress relaxation are the primary molecular mechanisms. The feature of their work is that they combined the Adam–Gibbs model of structural relaxation and a modified Eyring model of viscous flow into a thermoviscoelastic framework. Castro et al. (2010) proposed another viscoelasticity model that couples the structural relaxation and temperature dependent viscoelastic behavior. Their model could investigate the effects of thermal rates on shape memory behaviors of amorphous SMPs well. At the same time, Srivastava et al. (2010) formulated a large-deformation constitutive theory to model the response of thermally actuated SMPs. By expanding the early viscoelastic method, Ghosh and Srinivasa have developed a series of important constitutive models for SMPs and obtained reasonable results (Ghosh and Srinivasa, 2011, 2013, 2014). To provide a simpler and more effective prediction method for SMPs, a succinct three-element model is presented by Li et al. (2015). Even though it is simple, their model is feasible to evaluate the thermomechanical properties of SMPs. Although all existing viscoelastic models above have passably described some certain behaviors of SMPs, they are failed to physically relate the SME to glass transition which is a very important phenomenon for the SMP materials. Thus, the models with a clearer physical implication should be developed.

A phenomenological formulation for SMPs used in phase transition modeling approach has a clearer physical meaning than the viscoelastic modeling. The phase transition modeling approach was first introduced by Liu et al. (2006). Their continuum model used internal variables and constraints to describe the transition between the two phases. The different kinds of phases are interchangeable and can transform into each other with the change of temperature. After that, many new models have been developed by extending the work of Liu et al. (2006). Chen and Lagoudas (2008a, b) presented a nonlinear constitutive model to describe the strain storage and stress recovery mechanism of SMPs under large deformation. At the same time, Qi et al. (2008) proposed a three-phase transition model which is more accurate than that of Liu's et al. model. In recent years, phase transition modeling approach has still been used by many other researchers to develop constitutive models of SMPs, such as Reese et al. (2010), Volk et al. (2010), Long et al. (2010), Xu and Li (2010), Gilormini and Diani (2012), Baghani et al. (2014), Gu et al. (2014), Moon et al. (2015) and Yang and Li (2015). The continuum models based on phase transition in previous studies can reasonably reflect the glass transition and SME, however, this kind of approach defines the constructive model without considering the viscosity and the time dependence. They did not include the time factor and could not describe the creep and stress relaxation of polymers.

Although both of the two modeling approaches have great significance for the development of SMPs, their disadvantages cannot be ignored. Under such circumstances, a reasonable model with clearer physical meaning which can better present ample and comprehensive behaviors of SMPs should be imperatively developed. Here, we propose a novel viscoelastic model based on multiplicative decompositions of the deformation gradient and also have taken the time factor into consideration. This model has a clearer physical meaning and can successfully represent both the phase transition phenomenon and viscoelasticity of SMPs. Unlike previous work, which are mainly based on a specific material and limited to small strain (within 10%), our newly-proposed viscoelastic model unifies constitutive model with SME and can not only be used for different materials, but also large strain problems. Good agreement between prediction results and existing experimental data can be observed through the model validation.

The paper is presented as follows. In Section 2, we develop a novel viscoelastic model based on multiplicative decompositions of the deformation gradient. One-dimensional form of the proposed model is presented in Section 3. Then, we give a summary of the progress of the parameters identification in Section 4 and use the introduced model to predict two testing examples in Section 5. Finally, we draw concluding remarks in Section 6.

2. Constitutive model

2.1. General description of the constitutive model

The SME of SMPs is described by a phase transition at transformation temperature. As a kind of polymer materials, SMPs are cross-linked structures which can maintain a macro shape of SMPs (Ratna and Karger-Kocsis, 2008) with different microstructures at different temperature ranges. When they are heated over the glass transition temperature T_g and an external load is applied, the polymer chains would be reoriented and the cross-linked network would be dislocated which display as a macro deformation. Upon cooling and keeping the macro deformation, a kind of reversible phase (secondary cross-links) will form among the oriented polymer network architectures. The secondary cross-links which are glassy domains for amorphous SMPs, can fix the deformed shape and lay a good foundation for SME (Leng et al., 2011). As SMPs are reheated to the high temperature, the secondary cross-links disappear and the macro shape will recover to original shape. To depict the phase transition phenomenon and the formation and disappearance of the secondary cross-links, we propose a novel viscoelastic model for SMPs based on multiplicative decompositions of the deformation gradient.

The biggest difference between the ordinary single structural viscoelastic model (*e.g.*, Tobushi et al. (1997, 2001)) and the proposed model is the different constitutive structures above and below the transformation temperature (as shown in Fig. 1). When the temperature is higher than the glass transition temperature T_g, the SMPs are in the rubbery state. Under short-term loadings, rubber is often treated as isotropic incompressible hyperelastic material, while in a long time loading, stress relaxation and creep should be taken into account. Thus a simple model for SMPs at rubbery state is proposed, as shown in Fig. 1(a). This model for SMPs at rubbery state is composed of two incompressible hyperelastic elements and a viscous damping element (Fig. 1(a)). It represents the rubbery phase which is responsible for the permanent shape at a temperature higher than T_g (*i.e.*, rubbery phase branch).

As the temperature decreases below T_g, the material turns into the glassy state. In the glassy state, a kind of reversible phase, the secondary cross-links may be formed in the local area of reticular structure of SMPs, which act as small locks. The secondary cross-links lock the material's reticular structure to fix the temporal shape at a temperature lower than T_g. When the temperature increases above T_g, the secondary cross-links disappear and permanent shape is recovered. The secondary cross-links can be considered as springs in parallel with viscous dampers. Similarly, two spring elements and a viscous damping element are introduced into the model to simulate the reversible phase – the secondary cross-links (as shown in reversible phase of Fig. 1(b)) (*i.e.*, reversible phase branch). The constitutive model for SMPs consists of a rubbery phase branch and a reversible phase branch placed in parallel at $T \leq T_g$, as shown in Fig. 1(b).

In the model, the effect of thermal expansion, which is assumed to be independent of the mechanical behavior, is also considered (as depicted in Fig. 1(a) and (b)).

2.2. *Stress and deformation description of overall model*

In the proposed model (as shown in Fig. 1), no matter in the rubbery state ($T > T_g$) or glassy state ($T \leq T_g$), the total thermomechanical deformation gradient of the material $\boldsymbol{F}$ can be decomposed into (Holzapfel, 2000; Lu and Pister, 1975):

$$\boldsymbol{F} = \boldsymbol{F}_M \boldsymbol{F}_T \tag{1}$$

where $\boldsymbol{F}_M$ and $\boldsymbol{F}_T$ are the mechanical and thermal deformation gradient, respectively.

When the temperature is higher than T_g, the SMPs are in the rubbery state. At this case, there only exists the rubbery phase branch. Then, the total mechanical deformation gradient $\boldsymbol{F}_M$ is expressed as:

$$\boldsymbol{F}_M = \boldsymbol{F}_{R2} \boldsymbol{F}_{V1} = \boldsymbol{F}_{R1} \tag{2}$$

where $\boldsymbol{F}_{R1}$ and $\boldsymbol{F}_{R2}$ are the deformation gradients of hyperelastic elements and $\boldsymbol{F}_{V1}$ is the deformation gradient of viscous element in the rubbery phase branch (as shown in Fig. 1(a)).

The total Cauchy stress of the model is:

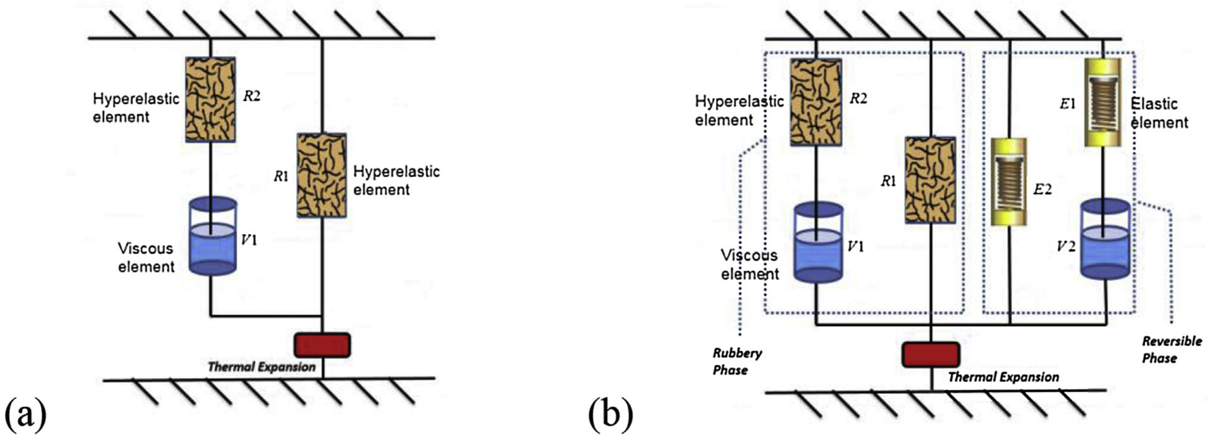

Fig. 1. Schematic representation of the proposed constitutive model: (a) Constitutive model for SMPs at $T > T_g$ (rubbery state); (b) Constitutive model for SMPs at $T \leq T_g$ (glassy state).

$$\boldsymbol{\sigma} = \boldsymbol{\sigma}_{R1} + \boldsymbol{\sigma}_{R2} \tag{3}$$

where $\boldsymbol{\sigma}_{R1}$ and $\boldsymbol{\sigma}_{R2}$ are the Cauchy stresses in the two hyperelastic elements. The Cauchy stress in the viscous element in the rubbery phase branch $\boldsymbol{\sigma}_{V1} = \boldsymbol{\sigma}_{R2}$.

When the temperature is lower than T_g, the material enters the glassy state. In the glassy state, this model is composed of a rubbery phase branch and a reversible phase branch arranged in parallel (Fig. 1(b)). In this state, Eq. (2) which describes the deformation gradients in the rubbery phase branch is also valid. The mechanical deformation gradient of the reversible phase branch $\boldsymbol{F}_{reversible}$ is:

$$\boldsymbol{F}_{reversible} = \boldsymbol{F}_{E1}\boldsymbol{F}_{V2} = \boldsymbol{F}_{E2} \tag{4}$$

where $\boldsymbol{F}_{E1}$ and $\boldsymbol{F}_{E2}$ are the deformation gradients of spring elements and $\boldsymbol{F}_{V2}$ is the deformation gradient of viscous element in the reversible phase branch (shown in Fig. 1(b)).

The reversible phase branch is formed when the temperature decreases to T_g. As in some previous studies (Ge et al., 2012; Rajagopal and Srinivasa, 1998a, b), it is assumed that the newly formed phase is formed in a stress-free (natural) configuration. At $T = T_g$, the newly formed reversible phase branch satisfies the condition $\boldsymbol{F}_{reversible} = 1$. Thus, the relationship between $\boldsymbol{F}_M$ and $\boldsymbol{F}_{reversible}$ can be expressed as:

$$\boldsymbol{F}_M = \boldsymbol{F}_{M-T_g}\boldsymbol{F}_{reversible} \tag{5}$$

where $\boldsymbol{F}_{M-T_g}$ is the total mechanical deformation gradient of the model at $T = T_g$.

In the glassy state, the total Cauchy stress of the model is rewritten as:

$$\boldsymbol{\sigma} = \boldsymbol{\sigma}_{R1} + \boldsymbol{\sigma}_{R2} + \boldsymbol{\sigma}_{E1} + \boldsymbol{\sigma}_{E2} \tag{6}$$

where $\boldsymbol{\sigma}_{E1}$ and $\boldsymbol{\sigma}_{E2}$ are the Cauchy stresses in the two spring elements. The Cauchy stress in the viscous element in the reversible phase branch $\boldsymbol{\sigma}_{V2} = \boldsymbol{\sigma}_{E1}$, and $\boldsymbol{\sigma}_{V1} = \boldsymbol{\sigma}_{R2}$ is also valid.

2.3. Rubbery phase

The stress and strain responses of SMPs are determined by the rubbery phase branch when there are no secondary crosslinks when $T > T_g$. As shown in Fig. 1(a), the rubbery phase branch consists of two incompressible hyperelastic elements and a viscous damping element.

To depict the hyperelasticity of SMPs in rubbery state, we use the Mooney–Rivlin model (Mooney, 1940; Rivlin, 1948) which is widely applied in rubbery material for the constitutive relation of the two hyperelastic elements. The strain energy density function for an incompressible Mooney–Rivlin solid is (Mooney, 1940):

$$W = C_{10}(I_1 - 3) + C_{01}(I_2 - 3) \tag{7}$$

where C_{10} and C_{01} are two material constants, I_1 and I_2 are the first and second invariant of the left Cauchy–Green deformation tensor $\boldsymbol{B}$:

$$I_1 = trace(\boldsymbol{B}) = \lambda_1^2 + \lambda_2^2 + \lambda_3^2 \tag{8}$$

$$I_2 = trace(\boldsymbol{B}\cdot\boldsymbol{B}) = (\lambda_1\lambda_2)^2 + (\lambda_2\lambda_3)^2 + (\lambda_3\lambda_1)^2 \tag{9}$$

where $\boldsymbol{B} = \boldsymbol{F}\boldsymbol{F}^T$ and λ_i are principal stretches. For an incompressible material, the volume ratio $J = \det(\boldsymbol{F}) = \lambda_1\lambda_2\lambda_3 = 1$.

From the Mooney–Rivlin model, the Cauchy stresses in the two incompressible hyperelastic elements can be given by:

$$\boldsymbol{\sigma}_{R1} = -p_{R1}\mathbf{I} + 2C_{10}^{R1}\boldsymbol{B}_{R1} - 2C_{01}^{R1}\boldsymbol{B}_{R1}^{-1} \tag{10}$$

$$\boldsymbol{\sigma}_{R2} = -p_{R2}\mathbf{I} + 2C_{10}^{R2}\boldsymbol{B}_{R2} - 2C_{01}^{R2}\boldsymbol{B}_{R2}^{-1} \tag{11}$$

where $\boldsymbol{B}_{R1}^{-1} = \boldsymbol{B}_{R1}\cdot\boldsymbol{B}_{R1} - I_1^{R1}\boldsymbol{B}_{R1} + I_2^{R1}\mathbf{I}$, $\boldsymbol{B}_{R2}^{-1} = \boldsymbol{B}_{R2}\cdot\boldsymbol{B}_{R2} - I_1^{R2}\boldsymbol{B}_{R2} + I_2^{R2}\mathbf{I}$, $p_{R1} = \frac{2}{3}(C_{10}^{R1}I_1^{R1} - C_{01}^{R1}I_2^{R1})$, $p_{R2} = \frac{2}{3}(C_{10}^{R2}I_1^{R2} - C_{01}^{R2}I_2^{R2})$. $\boldsymbol{\sigma}_{R1}$ and $\boldsymbol{\sigma}_{R2}$ are the stresses in the two hyperelastic elements (denoted by subscript *R1* and *R2*), the material constants, invariants and deformation tensors (denoted by subscript or superscript *R1* and *R2*) represent their values in the two hyperelastic elements, respectively. **I** is the second order unit tensor.

For the viscous damping element in the rubbery phase branch, we assume that the viscous damping is Newton fluid, the viscous stretch rate of the viscous damping element $\boldsymbol{D}_{V1}$ can be obtained:

$$\boldsymbol{D}_{V1} = \frac{1}{\eta_1}\boldsymbol{M}_{V1} \tag{12}$$

where η_1 is the viscosity of the viscous damping element in the rubbery phase branch and $\boldsymbol{M}_{V1}$ is the Mandel stress of this element.

In the case of isotropic material behavior and evolution equations of the form of Eq. (12), only the symmetric part of the viscous spatial velocity gradient is defined, $\boldsymbol{L}_{V1} = \dot{\boldsymbol{F}}_{V1}\boldsymbol{F}_{V1}^{-1}$. $\boldsymbol{M}_{V1}$ is independent on the rotation tensor and the spin tensor, then we have:

$$\boldsymbol{D}_{V1} = \dot{\boldsymbol{F}}_{V1}\boldsymbol{F}_{V1}^{\boldsymbol{-1}} \tag{13}$$

In the viscous damping element, the relationships among the Mandel stress, the second Piola-Kirchoff stress $\boldsymbol{S}_{V1}$ and the Cauchy stress $\boldsymbol{\sigma}_{V1}$ are:

$$\boldsymbol{M}_{V1} = \boldsymbol{C}_{V1}\boldsymbol{S}_{V1} \text{ and } \boldsymbol{S}_{V} = j_{V1}\boldsymbol{F}_{V1}^{-1}\boldsymbol{\sigma}_{V1}\boldsymbol{F}_{V1}^{-T} \tag{14}$$

where $\boldsymbol{C}_{V1} = \boldsymbol{F}_{V1}^{T}\boldsymbol{F}_{V1}$ is the right Cauchy–Green deformation tensor and $j_{V1} = 1/J_{V1} = 1/\det(\boldsymbol{F}_{V1})$.

2.4. Reversible phase (secondary cross-links)

When the material is in the glassy state ($T \le T_g$), the model is composed of a rubbery phase branch and a reversible phase branch. The rubbery phase branch has been established in section 2.3. In this section, we constitute the each part of the reversible phase branch.

The viscous damping element in the reversible phase branch is also assumed as Newton fluid, thus, the viscous stretch rate $\boldsymbol{D}_{V2}$ is:

$$\boldsymbol{D}_{V2} = \frac{1}{\eta_2}\boldsymbol{M}_{V2} \tag{15}$$

where η_2 is the viscosity of the viscous damping element in the reversible phase branch and $\boldsymbol{M}_{V2}$ is the Mandel stress of this element.

Similar with Eqs. (13) and (14), we have:

$$\boldsymbol{D}_{V2} = \dot{\boldsymbol{F}}_{V2}\boldsymbol{F}_{V2}^{-1} \tag{16}$$

$$\boldsymbol{M}_{V2} = \boldsymbol{C}_{V2}\boldsymbol{S}_{V2} \text{ and } \boldsymbol{S}_{V2} = j_{V2}\boldsymbol{F}_{V2}^{-1}\boldsymbol{\sigma}_{V2}\boldsymbol{F}_{V2}^{-T} \tag{17}$$

where $\boldsymbol{M}_{V2}$, $\boldsymbol{S}_{V2}$ and $\boldsymbol{\sigma}_{V2}$ are the Mandel stress, second Piola-Kirchoff stress and Cauchy stress in the viscous damping element in the reversible phase branch and $j_{V2} = 1/J_{V2} = 1/\det(\boldsymbol{F}_{V2})$.

For the two spring elements in the reversible phase branch, we introduce a corner mark i in parentheses to distinguish parameters of the two spring elements (*i.e.*, $i = E1$ and $i = E2$ correspond to element $E1$ and element $E2$, respectively) and consider the Hencky finite hyperelastic equation to describe them. Hencky strain is a favored measure for large deformation where principal directions of strains rotate (Onaka, 2010), then we have (Bruhns et al., 2002; Hencky, 1928):

$$\boldsymbol{\tau}_i = \Lambda_i(\ln J_i)\boldsymbol{1} + 2\mu_i\boldsymbol{h}_i \tag{18}$$

where Λ_i and μ_i are the classical Lamé elastic constants, $\boldsymbol{\tau}_i$ is the Kirchhoff stress tensor, which can be expressed by the volume ratio J_i and the Cauchy stress tensor $\boldsymbol{\sigma}_i$, $\boldsymbol{\tau}_i = J_i\boldsymbol{\sigma}_i$, and $\boldsymbol{h}_i$ is the Hencky's logarithmic strain tensor.

The Hencky's logarithmic strain tensor $\boldsymbol{h}_i$ is defined as:

$$\boldsymbol{h}_i = \frac{1}{2}\ln\boldsymbol{B}_i \tag{19}$$

where $\boldsymbol{B}_i = \boldsymbol{F}_i\boldsymbol{F}_i^{T}$.

For easier use of the Hencky equation, we rewrite Eq. (18) into component wise schemes. Suppose that the reference configuration of any Hencky material point is at $\boldsymbol{X}$, and the current configuration is at $\boldsymbol{x}$. Then, let $\boldsymbol{E}_X$, $\boldsymbol{E}_Y$ and $\boldsymbol{E}_Z$ be a reference rectangular Cartesian basis and let $\boldsymbol{e}_x$, $\boldsymbol{e}_y$ and $\boldsymbol{e}_z$ be a current rectangular Cartesian basis. The deformation gradient $\boldsymbol{F}_i$ is:

$$\boldsymbol{F}_i = \lambda_x^i\boldsymbol{e}_x \otimes \boldsymbol{E}_X + \lambda_y^i\boldsymbol{e}_y \otimes \boldsymbol{E}_Y + \lambda_z^i\boldsymbol{e}_z \otimes \boldsymbol{E}_Z \tag{20}$$

where λ_x^i, λ_y^i and λ_z^i are stretches in the three current coordinate axes directions, respectively.

The left Cauchy–Green deformation tensor $\boldsymbol{B}_i = \boldsymbol{F}_i\boldsymbol{F}_i^T$ becomes:

$$\boldsymbol{B}_i = \left(\lambda_x^i\right)^2 \boldsymbol{e}_x \otimes \boldsymbol{e}_x + \left(\lambda_y^i\right)^2 \boldsymbol{e}_y \otimes \boldsymbol{e}_y + \left(\lambda_z^i\right)^2 \boldsymbol{e}_z \otimes \boldsymbol{e}_z \tag{21}$$

The Hencky strain tensor $\boldsymbol{h}_i$ can be obtained from its definition (Eq. (19)):

$$\boldsymbol{h}_i = \ln\left(\lambda_x^i\right) \boldsymbol{e}_x \otimes \boldsymbol{e}_x + \ln\left(\lambda_y^i\right) \boldsymbol{e}_y \otimes \boldsymbol{e}_y + \ln\left(\lambda_z^i\right) \boldsymbol{e}_z \otimes \boldsymbol{e}_z \tag{22}$$

The volume ratio J_i is:

$$J_i = \det(\boldsymbol{F}_i) = \lambda_x^i \lambda_y^i \lambda_z^i \tag{23}$$

For the isotropic Hencky material, the Cauchy stress tensor $\boldsymbol{\sigma}_i$ is coaxial with the left Cauchy–Green deformation tensor $\boldsymbol{B}_i$. Therefore, $\boldsymbol{\sigma}_i$ can be written as:

$$\boldsymbol{\sigma}_i = \sigma_x^i \boldsymbol{e}_x \otimes \boldsymbol{e}_x + \sigma_y^i \boldsymbol{e}_y \otimes \boldsymbol{e}_y + \sigma_z^i \boldsymbol{e}_z \otimes \boldsymbol{e}_z \tag{24}$$

where σ_x^i, σ_y^i and σ_z^i are the stress components in the three current coordinate axes directions, respectively.

The classical Lamé elastic constants Λ_i and μ_i in Eq. (18) can be replaced by:

$$\Lambda_i = \frac{\nu_i E_i}{(1+\nu_i)(1-2\nu_i)} \text{ and } \mu_i = \frac{E_i}{2(1+\nu_i)} \tag{25}$$

where E_i is the Young's modulus and ν_i is the Poisson ratio.

Inserting Eqs. (22–25) into Eq. (18), we have:

$$\begin{cases} J_i\sigma_x^i = \dfrac{E_i}{(1-2\nu_i)(1+\nu_i)}\left[(1-\nu_i)\ln\lambda_x^i + \nu_i\left(\ln\lambda_y^i + \ln\lambda_z^i\right)\right] \\ J_i\sigma_y^i = \dfrac{E_i}{(1-2\nu_i)(1+\nu_i)}\left[(1-\nu_i)\ln\lambda_y^i + \nu_i\left(\ln\lambda_x^i + \ln\lambda_z^i\right)\right] \\ J_i\sigma_z^i = \dfrac{E_i}{(1-2\nu_i)(1+\nu_i)}\left[(1-\nu_i)\ln\lambda_z^i + \nu_i\left(\ln\lambda_y^i + \ln\lambda_x^i\right)\right] \end{cases} \tag{26}$$

Eq. (26) provides the component wise schemes of governing equations for the two spring elements (*i.e.*, $i = E1$ and $i = E2$ correspond to element $E1$ and element $E2$, respectively).

2.5. Thermal deformation

Without loss of generality, we assumed that the thermal expansion and contraction effect are isotropic and independent of the mechanical properties. Thus, the thermal deformation gradient $\boldsymbol{F}_T$ becomes:

$$\boldsymbol{F}_T = J_T^{1/3}\boldsymbol{1} \tag{27}$$

where J_T is the volume ratio due to thermal deformation and is defined as:

$$J_T = \frac{V(T)}{V_0} \tag{28}$$

where $V(T)$ is the volume at temperature T and V_0 is the reference volume at a selected reference temperature T_0 ($T_0 > T_g$).

For many polymers, the coefficient of thermal expansion (CTE) is different when the materials are in different states. Supposed that in the rubbery state, the CTE of polymers is α_R and in the glassy state, the CTE of polymers is α_G. Then we can get the volume ratio in different material states as follows.

When the material is in the rubbery state ($T > T_g$):

$$J_T = \frac{V(T)}{V_0} = [1 + \alpha_R(T - T_0)]^3 \approx 1 + 3\alpha_R(T - T_0) \tag{29}$$

When the material is in the glassy state ($T \le T_g$):

$$J_T = \frac{V(T)}{V_0} = \left[1 + \alpha_R(T_g - T_0) + \alpha_G(T - T_g)\right]^3 \approx 1 + 3\alpha_R(T_g - T_0) + 3\alpha_G(T - T_g) \tag{30}$$

2.6. Time-discrete form of the constitutive model

In this sub-section, we investigate the numerical solution of the proposed constitutive model. The total stress is complicated because the deformation gradients of viscous elements are unknown except the mechanical deformation $\boldsymbol{F}_M$. Therefore, the total stress and the variables are updated from the mechanical deformation history. We subdivide the time interval of interest $[0, t]$ into sub-increments. For a generic advancement of time $[t_n, t_{n+1}]$, the stress and deformation tensors are denoted by subscript n at time t_n and $n+1$ at time t_{n+1}, respectively.

When the SMPs are in the rubbery state, from Eqs. (12–14) as well as $\boldsymbol{\sigma}_{V1} = \boldsymbol{\sigma}_{R2}$, we can obtain the relationship between $\boldsymbol{F}_{V1}$ and $\boldsymbol{F}_{R2}$ as:

$$\boldsymbol{F}_{R2}\boldsymbol{L}_{V1}\boldsymbol{F}_{R2}^T = \frac{\boldsymbol{B}_{R2}\boldsymbol{\sigma}_{R2}}{\eta_1} \tag{31}$$

Discretization of the evolution equation (31) by the so-called exponential mapping (Chen et al., 2014; Reese and Govindjee, 1998) gives:

$$\frac{1}{2} ln\left(\boldsymbol{B}_{R2}^{n+1}\right) = \Delta t \frac{\boldsymbol{\sigma}_{R2}^n}{\eta_1} + \frac{1}{2} ln\left(\boldsymbol{B}_{R2}^{trial}\right) \tag{32}$$

Where $\boldsymbol{B}_{R2}^{trial} = (\boldsymbol{F}_M^{n+1})\cdot(\boldsymbol{C}_{V1}^n)^{-1}\cdot(\boldsymbol{F}_M^{n+1})^T = (\boldsymbol{F}_M^{n+1})\cdot(\boldsymbol{F}_M^n)^{-1}\cdot(\boldsymbol{B}_{R2}^n)\cdot(\boldsymbol{F}_M^n)^{-T}\cdot(\boldsymbol{F}_M^{n+1})^T$ is the coupling term of $\boldsymbol{B}_{R2}$ between the time t_n and the time t_{n+1}.

The stress of hyperelastic element *R2* at the time t_n is:

$$\boldsymbol{\sigma}_{R2}^n = -p_{R2}^n\mathbf{I} + 2C_{10}^{R2}\boldsymbol{B}_{R2}^n - 2C_{01}^{R2}\left(\boldsymbol{B}_{R2}^n\right)^{-1} \tag{33}$$

Substituting Eq. (33) into Eq. (32), $\boldsymbol{B}_{R2}$ can be solved with the initial condition that $\boldsymbol{B}_{R2}(t=0) = \mathbf{I}$.

From Eq. (10) and $\boldsymbol{F}_{R1} = \boldsymbol{F}_M$, the stress of hyperelastic element *R1* at the time t_n is

$$\boldsymbol{\sigma}_{R1}^n = -p_M^n\mathbf{I} + 2C_{10}^{R2}\boldsymbol{B}_M^n - 2C_{01}^{R2}\left(\boldsymbol{B}_M^n\right)^{-1} \tag{34}$$

Thus, the iteration the total Cauchy stress of the model, in the rubbery state, is

$$\boldsymbol{\sigma}^n = \boldsymbol{\sigma}_{R1}^n + \boldsymbol{\sigma}_{R2}^n \tag{35}$$

When the SMPs are in the glassy state, from Eqs. (15–17) as well as $\boldsymbol{\sigma}_{V2} = \boldsymbol{\sigma}_{E1}$, we can obtain the relationship between $\boldsymbol{F}_{V2}$ and $\boldsymbol{F}_{E1}$ as:

$$\boldsymbol{F}_{E1}\boldsymbol{L}_{V2}\boldsymbol{F}_{E1}^T = \frac{\boldsymbol{B}_{E1}\boldsymbol{\sigma}_{E1}}{\eta_2} \tag{36}$$

Similar with Eq. (32), discretization of the evolution equation (36) can be obtained as:

$$\frac{1}{2} ln\left(\boldsymbol{B}_{E1}^{n+1}\right) = \Delta t \frac{\boldsymbol{\sigma}_{E1}^n}{\eta_2} + \frac{1}{2} ln\left(\boldsymbol{B}_{E1}^{trial}\right) \tag{37}$$

Where $\boldsymbol{B}_{E1}^{trial} = (\boldsymbol{F}_{reversible}^{n+1})\cdot(\boldsymbol{C}_{V2}^n)^{-1}\cdot(\boldsymbol{F}_{reversible}^{n+1})^T = (\boldsymbol{F}_{reversible}^{n+1})\cdot(\boldsymbol{F}_{reversible}^{n+1})^{-1}\cdot(\boldsymbol{B}_{E1}^n)\cdot(\boldsymbol{F}_{reversible}^n)^{-T}\cdot(\boldsymbol{F}_{reversible}^{n+1})^T$ is the coupling term of $\boldsymbol{B}_{E1}$ between the time t_n and the time t_{n+1}, $\boldsymbol{F}_{reversible}^n = \boldsymbol{F}_{M-T_g}^{-1}\boldsymbol{F}_M^n$.

We come to the stress of spring element *E1* from Eqs. (18) and (19) at the time t_n:

$$\boldsymbol{\sigma}_{E1}^n = \frac{1}{J_{E1}^n}\left(\Lambda_{E1}\left(\ln J_{E1}^n\right)\boldsymbol{1} + 2\mu_{E1}\,\ln\left(\boldsymbol{B}_{E1}^n\right)^{1/2}\right) \tag{38}$$

Substituting Eq. (38) into Eq. (37), $\boldsymbol{B}_{E1}$ can be solved with the initial condition that $\boldsymbol{B}_{E1}(T = T_g) = \mathbf{I}$.

The stress of spring element *E2* at the time t_n can be obtained from Eqs. (18) and (19) as well as $\boldsymbol{F}_{E2} = \boldsymbol{F}_{reversible} = \boldsymbol{F}_{M-T_g}^{-1}\boldsymbol{F}_M$,

$$\boldsymbol{\sigma}_{E2}^{n} = \frac{1}{J_{reversible}^{n}} \left(\Lambda_{E1} \left(\ln J_{reversible}^{n} \right) \boldsymbol{1} + 2\mu_{E1} \ln \left(\boldsymbol{B}_{reversible}^{n} \right)^{1/2} \right) \tag{39}$$

As a result, the iteration the total Cauchy stress of the model, in the glassy state, is

$$\boldsymbol{\sigma}^{n} = \boldsymbol{\sigma}_{R1}^{n} + \boldsymbol{\sigma}_{R2}^{n} + \boldsymbol{\sigma}_{E1}^{n} + \boldsymbol{\sigma}_{E2}^{n} \tag{40}$$

In this section, a three-dimensional (3D) thermomechanical constitutive model and corresponding elements of the model have been established. To validate the model by comparing simulated results of the model with uniaxial tensile experiments, we will apply the 3D model to uniaxial tensile state in section 3. Furthermore, the model parameters are determined and the verification results are carried out in successive sections.

3. One-dimensional form for the proposed model

To verify our model, we compare the model simulation results with the experiments available in the literatures (Tobushi et al., 1997, 2001; McClung et al., 2013). The experiments which implement the shape memory cycle are normally in uniaxial tension state. Therefore, we provide a summary of one-dimensional form for the proposed model in this section.

3.1. The constitutive relations of each element of the proposed model in uniaxial tension

For the two hyperelastic elements which are considered as the incompressible Mooney–Rivlin material, the Cauchy stress under uniaxial elongation can be calculated as:

$$\sigma_{R1} = 2C_{10}^{R1} \left(\lambda_{R1}^{2} - \lambda_{R1}^{-1} \right) + 2C_{01}^{R1} \left(\lambda_{R1} - \lambda_{R1}^{-2} \right) \tag{41}$$

$$\sigma_{R2} = 2C_{10}^{R2} \left(\lambda_{R2}^{2} - \lambda_{R2}^{-1} \right) + 2C_{01}^{R2} \left(\lambda_{R2} - \lambda_{R2}^{-2} \right) \tag{42}$$

where λ_{R1} and λ_{R2} are the stretches of the two hyperelastic elements.

For the viscous damping element in the rubbery phase branch, apply Eqs. (12–14) to uniaxial tension, the Cauchy stress of this viscous damping element can be obtained:

$$\sigma_{V1} = \eta_{1} \frac{\dot{\lambda}_{V1}}{\lambda_{V1}} \tag{43}$$

where λ_{V1} is the stretch and $\dot{\lambda}_{V1}$ is the time derivative of stretch.

In the same way, the Cauchy stress of the viscous damping element in the reversible phase branch can also be obtained:

$$\sigma_{V2} = \eta_{2} \frac{\dot{\lambda}_{V2}}{\lambda_{V2}} \tag{44}$$

where λ_{V2} and $\dot{\lambda}_{V2}$ are the stretch and the time derivative of stretch of the viscous damping element in the reversible phase branch, respectively.

For the two spring elements, the constitutive relation of a 1D spring is (Sweeney et al., 1999; Wong et al., 2011):

$$\sigma_{E1} = E_{1} \ln(\lambda_{E1}) \tag{45}$$

$$\sigma_{E2} = E_{2} \ln(\lambda_{E2}) \tag{46}$$

where λ_{E1} and λ_{E2} are the stretches of the two spring elements.

3.2. Overall model description for uniaxial tension

First, we can obtain the total deformation from Eq. (1). Applying Eq. (1) to uniaxial tension, the total stretch of the model λ is obtained as:

$$\lambda = \lambda_{M} \lambda_{T} \tag{47}$$

where λ_{M} is the total mechanical stretch and λ_{T} is the thermal stretch.

At $T > T_g$, the constitutive model for SMPs is presented as Fig. 1(a), from Eqs. (2) and (3), the total mechanical stretch and total Cauchy stress of the model can be obtained as:

$$\lambda_M = \lambda_{R2}\lambda_{V1} = \lambda_{R1} \tag{48}$$

$$\sigma = \sigma_{R1} + \sigma_{R2} = \sigma_{R1} + \sigma_{V1} \tag{49}$$

where σ_{R1}, σ_{R2} and σ_{V1} are the Cauchy stresses in the three elements in the rubbery phase branch. The relationships between these stresses and their respective deformation are given in Eqs. (41–43).

At $T \le T_g$, the constitutive model for SMPs is presented as Fig. 1(b). In this state, Eq. (48) which describes the deformations in the rubbery phase branch is also valid. From Eqs. (4) and (5), the mechanical stretch of the reversible phase branch $\lambda_{reversible}$ and total mechanical stretch λ_M can be expressed as:

$$\lambda_{reversible} = \lambda_{E1}\lambda_{V2} = \lambda_{E2} \tag{50}$$

$$\lambda_M = \lambda_{M-T_g}\lambda_{reversible} \tag{51}$$

where λ_{M-T_g} is the total mechanical stretch of the model at $T = T_g$.

Because of the existence of reversible phase branch, the total Cauchy stress of the model is rewritten as:

$$\sigma = \sigma_{R1} + \sigma_{R2} + \sigma_{E1} + \sigma_{E2} \tag{52}$$

As previously mentioned, the above stresses of each part are given in section 3.1. It follows from the series arrangement of the hyperelastic element ($R2$) and the viscous element ($V1$) in the rubbery phase branch that: $\sigma_{V1} = \sigma_{R2}$ and from the series arrangement of the spring element ($E1$) and the viscous element ($V2$) in the reversible phase branch that: $\sigma_{V2} = \sigma_{E1}$.

4. Determination of the model parameters

In the proposed model, the parameters of six model elements and the CTE of materials need to be determined. In this section, we give a summary of the progress of the parameters identification.

For an incompressible Mooney–Rivlin material, the two C_{10} and C_{01} satisfy $\mu_R = 2(C_{10} + C_{01})$, where μ_R is the initial shear modulus of hyperelastic element. μ_R can be replaced by $\mu_R = \frac{E_R}{2(1+\nu_R)}$ with E_R the initial tensile modulus and ν_R the Poisson ratio. For the two incompressible hyperelastic elements $\nu_R = 0.5$ and $E_R = 6(C_{10} + C_{01})$. Using an empirical formula $C_{01} = 0.25C_{10}$, such that $C_{10} = E_R/7.5,\ \ C_{01} = E_R/30$. Therefore, we only need to determine the modulus of the two hyperelastic elements E_{R1} and E_{R2}, and then the Mooney–Rivlin model constants can be obtained.

In general, there are six parameters E_{R1}, E_{R2}, η_1, E_1, E_2 and η_2 in the rubbery phase branch and the reversible phase branch need to be identified. The modulus and tensile properties of SMPs are influence by the temperature. In the same way, the above model parameters (E_{R1}, E_{R2}, η_1, E_1, E_2 and η_2) are dependent on the temperature. To determine these temperature-dependent model parameters, we adopt the uniaxial tensile tests of SMPs at different temperatures which have been carried out in many literatures.

At $T > T_g$, the model only has three elements in the rubbery phase branch which represent the primary cross-links of SMPs. The parameters of the rubbery phase branch E_{R1}, E_{R2} and η_1 can be obtained by using an empirically definition (Tobushi et al., 2001):

$$x = x_g \exp\left[a_x\left(\frac{T_g}{T} - 1\right)\right] \tag{53}$$

where x denote the parameters E_{R1}, E_{R2} and η_1, x_g is the value of x at temperature $T = T_g$, a_x is the exponent for each coefficient x.

Based on the uniaxial tensile tests of SMPs at a series of temperatures above T_g, the temperature-dependent parameters $E_{R1}(T)$, $E_{R2}(T)$ and $\eta_1(T)$ would be determined.

When the temperature reaches T_g, the reversible phase branch displaying the secondary cross-links would be introduced to the model. It is reasonable to assume that the secondary cross-links start to form at $T = T_g$, and the newly formations would be gradually increased with the temperature decreased continuously. To describe the continuous phase transition process, we introduce a frozen fraction which can characterize the fraction of the frozen phase (Liu et al., 2006): $\phi_f(T) = 1 - \frac{1}{1+c(T_r-T)^n}$, where T_r is the reference temperature, c and n are two undetermined parameters. The frozen phase is frozen because the secondary cross-links lock the material's reticular structure. The more the secondary cross-links lock, the larger the fraction of the frozen phase becomes. Hence, we assume that the model parameters in the reversible phase branch and the frozen fraction change approximately in the same way. The three temperature-dependent parameters $E_1(T)$, $E_2(T)$, $\eta_2(T)$ are defined as:

Table 1
Model parameters in the rubbery phase branch adopted from experiments reported by Tobushi et al. (1997, 2001).

Coefficients	$T > 343K$	$343K > T > 313K$	$T \leq 313K$
$C_{10}^{R1}(MPa)$	1.8	$3.5829\exp\left[7.8706\left(\frac{313K}{T}-1\right)\right]$	3.5829
$C_{01}^{R1}(MPa)$	0.45	$0.8957\exp\left[7.8706\left(\frac{313K}{T}-1\right)\right]$	0.8957
$C_{10}^{R2}(MPa)$	1.75	$16.3245\exp\left[25.5312\left(\frac{313K}{T}-1\right)\right]$	16.3245
$C_{01}^{R2}(MPa)$	0.4375	$4.0811\exp\left[25.5312\left(\frac{313K}{T}-1\right)\right]$	4.0811
$\eta_1(MPa{*}s)$	964.078	$11740.215\exp\left[28.5788\left(\frac{313K}{T}-1\right)\right]$	11740.215

$$E_1(T) = E_1\left(1 - \frac{1}{1 + c_{E1}(T_g - T)^{n_{E1}}}\right) \tag{54}$$

$$E_2(T) = E_2\left(1 - \frac{1}{1 + c_{E2}(T_g - T)^{n_{E2}}}\right) \tag{55}$$

$$\eta_2(T) = \eta_2\left(1 - \frac{1}{1 + c_{\eta 2}(T_g - T)^{n_{\eta 2}}}\right) \tag{56}$$

where E_1, E_2 and η_2 are limited values of the three parameters, $c_{E1}, n_{E1}, c_{E2}, n_{E2}, c_{\eta 2}$ and $n_{\eta 2}$ are the undetermined parameters for the three parameter definitions which can be determined by fitting the experimental data. At $T = T_g$, the secondary cross-links start to form and the values of the parameters are zero; as the temperature decreases, the more secondary cross-links form and the values of the parameters will be higher and approach to the limited values gradually.

The model parameters in the rubbery phase branch have been determined before, so the temperature-dependent parameters $E_1(T)$, $E_2(T)$ and $\eta_2(T)$ can be determined by fitting the uniaxial tensile test data of SMPs at temperatures lower T_g.

The CTE of materials which is given in the literatures (Tobushi et al., 1997, 2001; McClung et al., 2013) and can be directly measured by the DMA machine. In this study, we adopt the available CTE of materials from pertinent literatures.

5. Results and discussion

In this section, we use the proposed model to predict two testing examples and compare the model predicted results with experimental data available in the literatures. The shape memory behavior of a polyurethane SMP with different pre-strain levels and shape memory cycle prediction of Veriflex-E epoxy SMP for large strain are investigated to validate this model.

5.1. Shape memory behavior of SMP with different pre-strain levels

To test the stability of the model, we simulate thermomechanical tests with several pre-strain levels reported by Tobushi et al. (1997, 2001). The parameters used in the model are shown in Tables 1 and 2. For this material, the CTE $\alpha_R = \alpha_G = 11.6 \times 10^{-5}K^{-1}$. Figs. 2–4 show the stress-strain curves, stress-temperature curves and strain-temperature curves in free strain recovery case with three different pre-strain ε_m, respectively. To compare model reproductions, the numerical simulation results of Tobushi et al. (1997, 2001) are illustrated in Figs. 2–4, too. It shows that our present simulated results are

Table 2
Model parameters in the reversible phase branch adopted from experiments reported by Tobushi et al. (1997, 2001).

Coefficients	$T > 328K$	$313K < T \leq 328K$	$T \leq 313K$
$E_1(MPa)$	0	$277758.5\left[1 - \frac{1}{1+1.87721\times10^{-5}(328K-T)^{1.81889}}\right]$	716.54324
$E_2(MPa)$	0	$1753.63504\left[1 - \frac{1}{1+3.38226\times10^{-4}(328K-T)^{1.16742}}\right]$	13.84114
$\eta_2(MPa{*}s)$	0	$41506500\left[1 - \frac{1}{1+1.05303\times10^{-5}(328K-T)^{1.99305}}\right]$	96284.99663

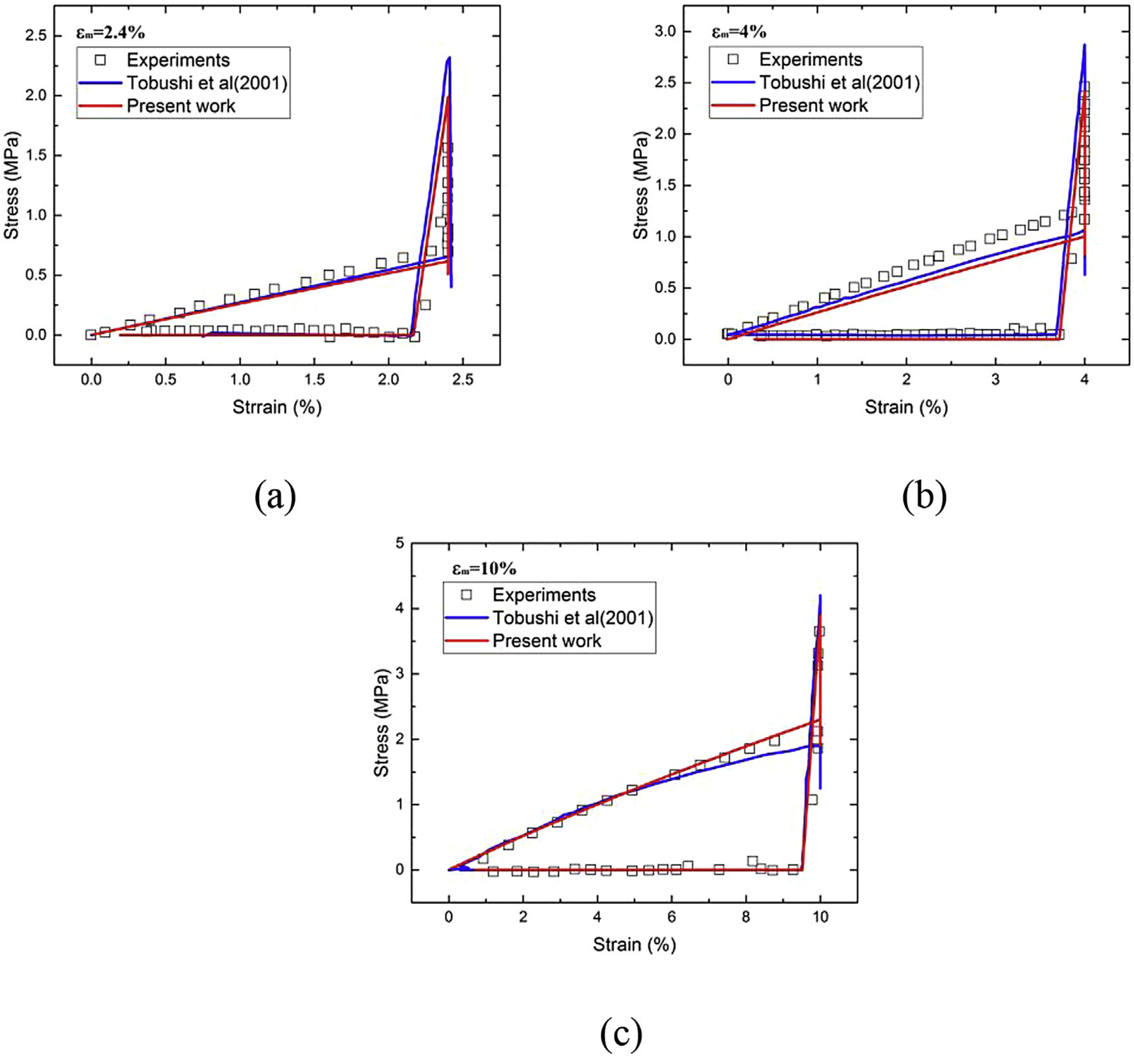

(a)

(b)

(c)

Fig. 2. Stress-strain curves: (a) $\varepsilon_m = 2.4\%$, (b) $\varepsilon_m = 4\%$, (c) $\varepsilon_m = 10\%$. Experiments reported by Tobushi et al. (1997) and Tobushi et al. (2001).

better according with the experimental observations than the predictions of Tobushi et al. (1997, 2001), indicating its feasibility to reproduce shape memory behavior of SMP with different pre-strain levels.

5.2. The shape memory cycle prediction for large strain (more than 10%)

In previous research work, most constitutive models of SMPs are based on a specific material and limited to small strain behavior which narrow the application of models. To show the wide applicability of our model, we perform the shape memory cycle prediction of another material (Veriflex-E epoxy SMP) for large strain (larger than 10%) and compare it with the experimental results in McClung et al. (2013). The experimental details can be found in McClung et al. (2013) and the model parameters used in this case are shown in Tables 3 and 4. For this material, $\alpha_R = 2.893 \times 10^{-4} K^{-1}$ and $\alpha_G = 3.498 \times 10^{-5} K^{-1}$.

In the experiment, the temperature of the SMP sample is artificially controlled. The temperature history over time in the shape memory cycle is presented in Fig. 5. To better understand the shape memory behavior, we divide a shape memory cycle into 5 processes based on the change of temperature (as shown in Figs. 5 and 6). In the process 1, the SMP sample is pre-tensioned to 60% strain and the strain is maintained for a while at 130 °C. In the process 2, the sample is cooled down to 25 °C while the constant strain is maintained. After cooling, the constant strain is held at 25 °C for 1 h in the process 3. In the initial stage of the process 4, the strain constraint condition is rapidly removed from the sample at 25 °C. Then, the sample is reheated from 25 °C to 130 °C. After the heating, the temperature is held at 130 °C for 1 h in the process 5.

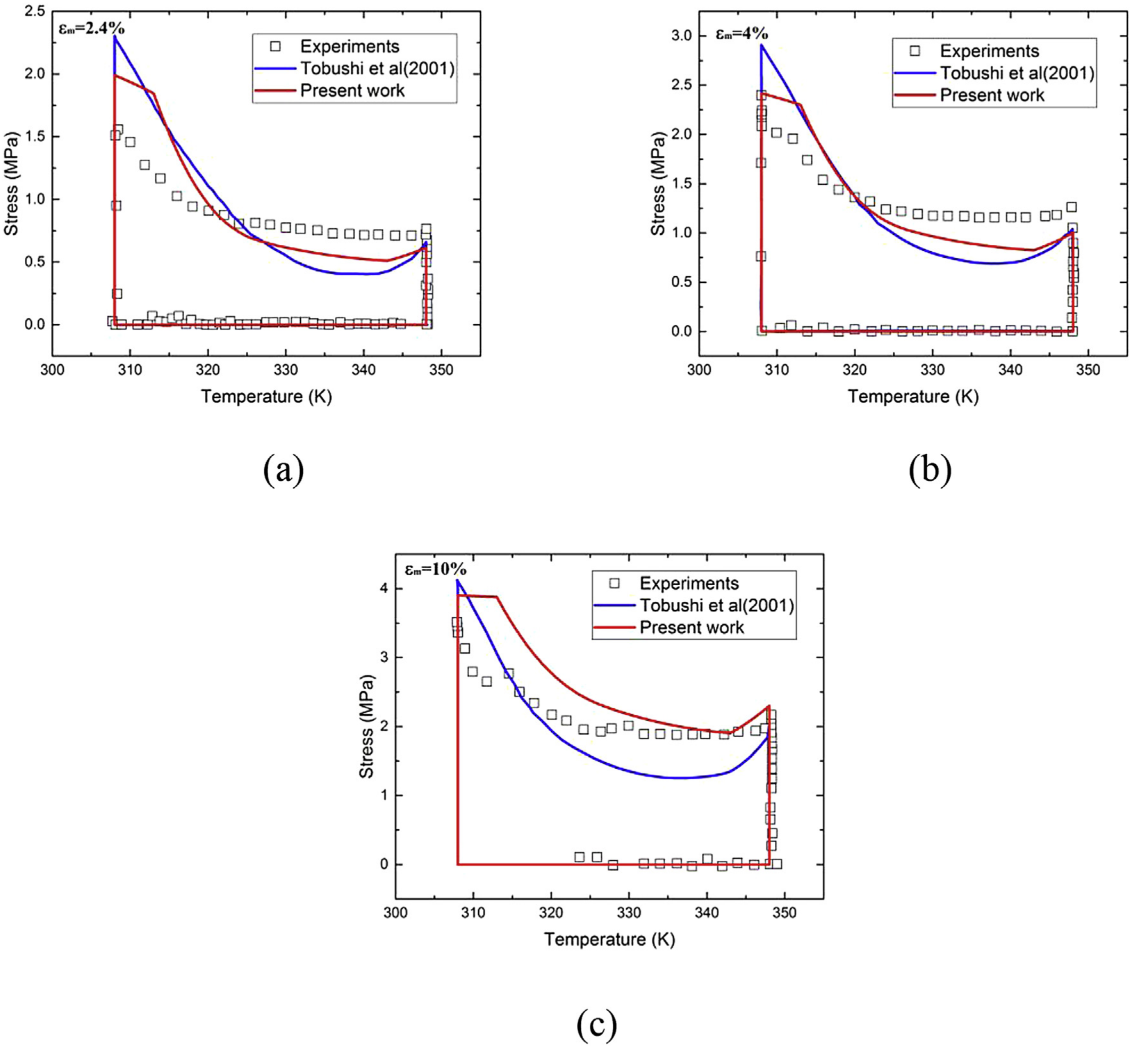

(a)

(b)

(c)

Fig. 3. Stress-temperature curves: (a) $\varepsilon_m = 2.4\%$, (*b*) $\varepsilon_m = 4\%$, (*c*) $\varepsilon_m = 10\%$. Experiments reported by Tobushi et al. (1997) and Tobushi et al. (2001).

Fig. 6 shows the comparison between the model prediction and experiment in free recovery shape memory cycle. From the comparison, we can see that the modeling results agree fairly well with the experimental data in reproducing the stress history and strain evolution. But there are some small discrepancies: (1) During the process 2, there is time-lag of the experiment with modeling results in stress evolution. And at the end of the process 2, the stress value of the model is larger than the experimental one. (2) During the process 3, the modeling stress decreases a little while the experimental stress continues to increase slowly. (3) During the late-stage of the process 4 and the initial stage of the process 5, there is time-lag of the experiment with modeling results in strain evolution.

The above discrepancy occurs in the processes of temperature change or at the beginning of temperature change completion, and the discrepancy mainly appears as time-lag of the experiment with modeling results. So we make a reasonable hypothesis that the practical temperature lags behind monitor temperature in time due to the realization of thermal equilibrium. By assuming this, we can see that in the process 2, the sample is cooled. The monitor temperature which is used in model simulation is always lower than practical temperature of sample and the modeling stress would be always higher than experimental stress. In the process 3, the sample is held at constant strain and constant temperature. In this holding process, the strain frozen and thermal deformation stop changing while the stress relaxation continue to exist. Thus, the stress should decrease in theory. In the experiment, at the end of the process 2, the actual temperature is not cooled to 25 °C yet. It would continue to drop to 25 °C in the holding process 3. Therefore, we observed that the experimental stress continues to increase slowly while the modeling stress decreases. Similarly, in the reheating process 4, the practical temperature lags behind monitor temperature and the strain recovery of experimental observation lags behind the modeling results.

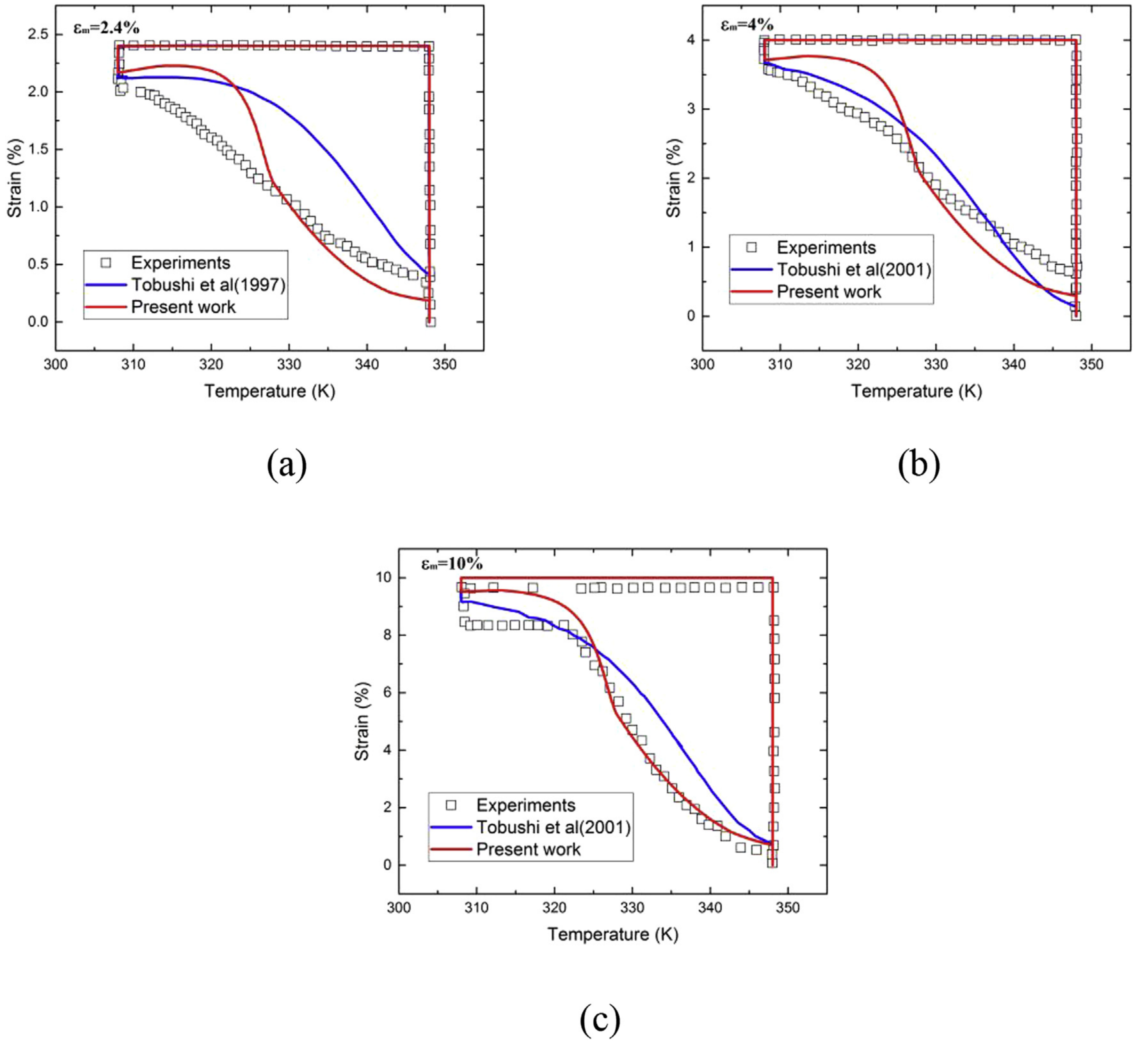

(a) (b)

(c)

Fig. 4. Strain-temperature curves: (a) $\varepsilon_m = 2.4\%$, (b) $\varepsilon_m = 4\%$, (c) $\varepsilon_m = 10\%$. Experiments reported by Tobushi et al. (1997) and Tobushi et al. (2001).

To revise these discrepancy caused by thermal lag, we make a left-ward shift (0.23 h) in the experimental stress-time curve and strain-time curve (as shown in Fig. 7). We mainly focus on the stress evolution in the processes 2 - 3 and the strain recovery in the processes 4 - 5. A good agreement between the model predictions and shifted experimental data is presented in Fig. 7, proving that our model can effectively predict the shape memory behavior of Veriflex-E epoxy SMP for large strain.

Table 3
Model parameters in the rubbery phase branch adopted from experiments reported by McClung et al. (2013).

Coefficients	$T > 368K$	$T \leq 368K$
$C_{10}^{R1}(MPa)$	$0.639216 \exp\left[24.86407\left(\frac{368K}{T} - 1\right)\right]$	0.639216
$C_{01}^{R1}(MPa)$	$0.159804 \exp\left[24.86407\left(\frac{368K}{T} - 1\right)\right]$	0.159804
$C_{10}^{R2}(MPa)$	$1.660024 \exp\left[94.18957\left(\frac{368K}{T} - 1\right)\right]$	1.660024
$C_{01}^{R2}(MPa)$	$0.415006 \exp\left[94.18957\left(\frac{368K}{T} - 1\right)\right]$	0.415006
$\eta_1(MPa{*}h)$	$0.16854 \exp\left[24.70961\left(\frac{368K}{T} - 1\right)\right]$	0.16854

Table 4
Model parameters in the reversible phase branch adopted from experiments reported by McClung et al. (2013).

Coefficients	$T > 368K$	$T \leq 368K$
$E_1(MPa)$	0	$1197.12235\left[1-\frac{1}{1+3.59017\times10^{-10}(368K-T)^{13.4335}}\right]$
$E_2(MPa)$	0	$2854.71345\left[1-\frac{1}{1+8.94004\times10^{-4}(368K-T)^{2.24521}}\right]$
$\eta_2(MPa{*}h)$	0	$171.6827\left[1-\frac{1}{1+4.19473\times10^{-5}(368K-T)^{4.54163}}\right]$

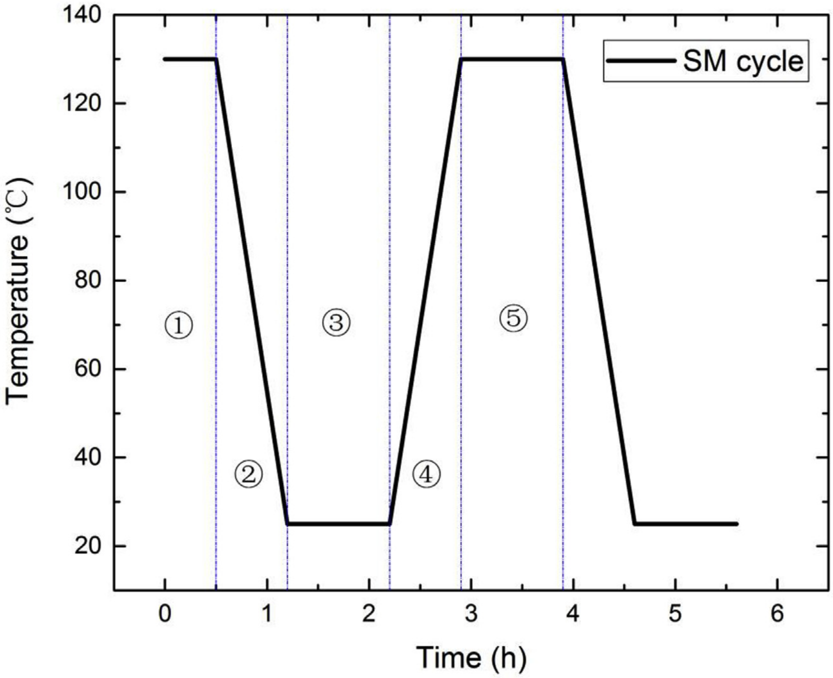

Fig. 5. Temperature-time history of the SMP sample in the shape memory cycle. Experiments reported by McClung et al. (2013).

5.3. Multiaxial loading case

In this sub-section, we simulate a multiaxial loading case (equal-biaxial force) to show the full capabilities of the proposed model under multiaxial loading path. The similar important works were investigated by Baghani et al. (2012). In this example, the main parameters as shown in Tables 1 and 2, are adopted. In the first loading step, the strains $\varepsilon_{11} = 0.1$ and $\varepsilon_{22} = 0.1$ with strain rate of $8.33 \times 10^{-3}s^{-1}$ are applied at an elevated temperature T_h. Then, we hold the strains ($\varepsilon_{11} = 0.1$, $\varepsilon_{22} = 0.1$) and decrease the temperature to a lower temperature T_l with cooling rate of 0.133 K/s. In third step, the strain constraint conditions are removed. After that, the specimen is in temporary shape. Finally, the SMP specimen is reheated to high temperature T_h under the free strain condition with heating rate of 0.0667 K/s. Through reproduction of above four loading steps, the stress-temperature curves, stress-strain curves and strain-temperature curves under equal-biaxial force case are depicted in Fig. 8.

From Fig. 8(a), it can be observed that the stresses (σ_{11}, σ_{22}) decrease in the early stage of cooling, then, increase around T_g and almost remain constant in the vicinity of T_h . It happens due to that the stress responses of the SMP are affected by three factors: stress relaxation, thermal strains and phase transition. Further studying Fig. 8(b) and c, we can find that after unloading, a temporary shape is maintained; and after reheating, some residual strains are remained in SMP.

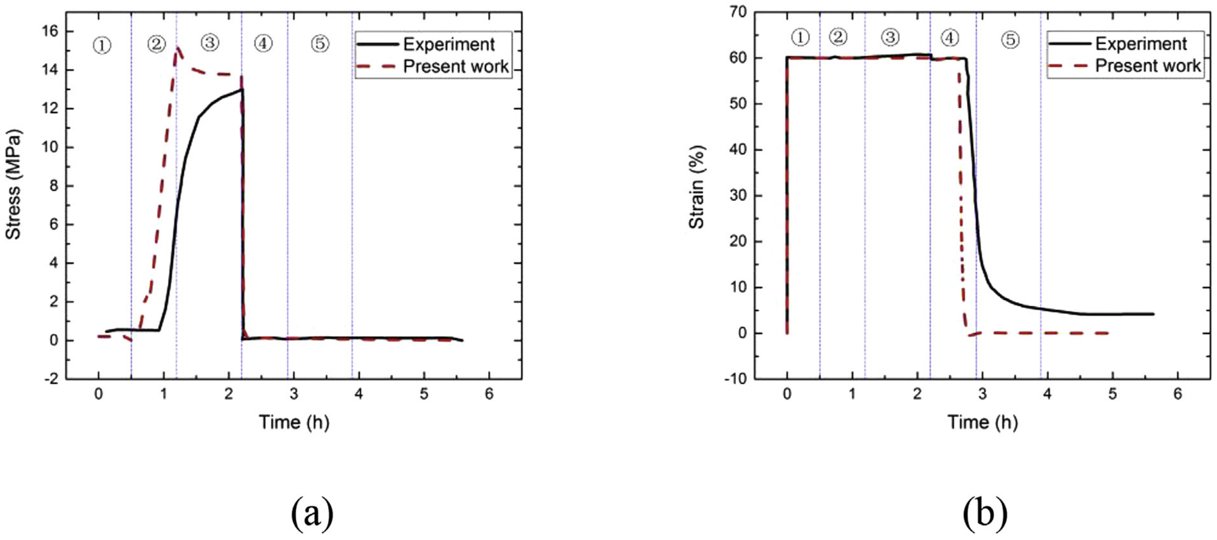

Fig. 6. The comparison between the model prediction and experiment in free recovery shape memory cycle: (a) the curves of stress-time, (b) the curves of strain-time. Experiments reported by McClung et al. (2013).

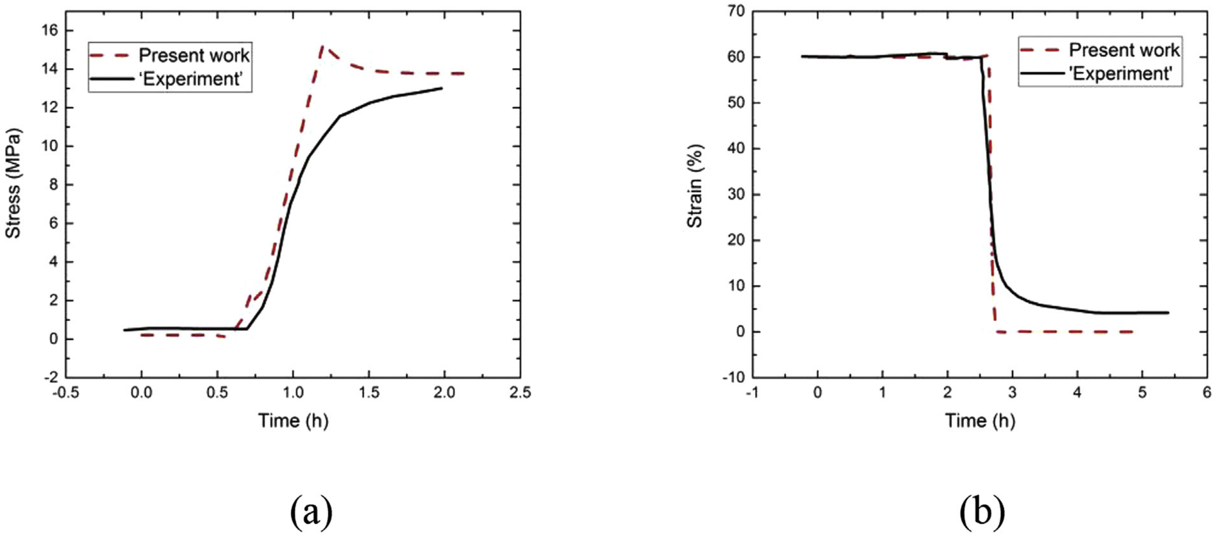

Fig. 7. The comparison between the model prediction and shifted experimental data: (a) the curves of stress-time, (b) the curves of strain-time. The left-ward shift value is 0.23 h. Experiments reported by McClung et al. (2013).

6. Concluding remarks

In present study, a novel viscoelastic model for shape memory polymers (SMPs) based on multiplicative thermoviscoelasticity is established for SMPs and is used to reproduce the SME of different shape memory materials. The simulated results are compared with available experimental results and a remarkable consistency between the model prediction and experimental data can be obtained. From the results and discussion, it demonstrated that the present model shows several advantages comparing with previous models:

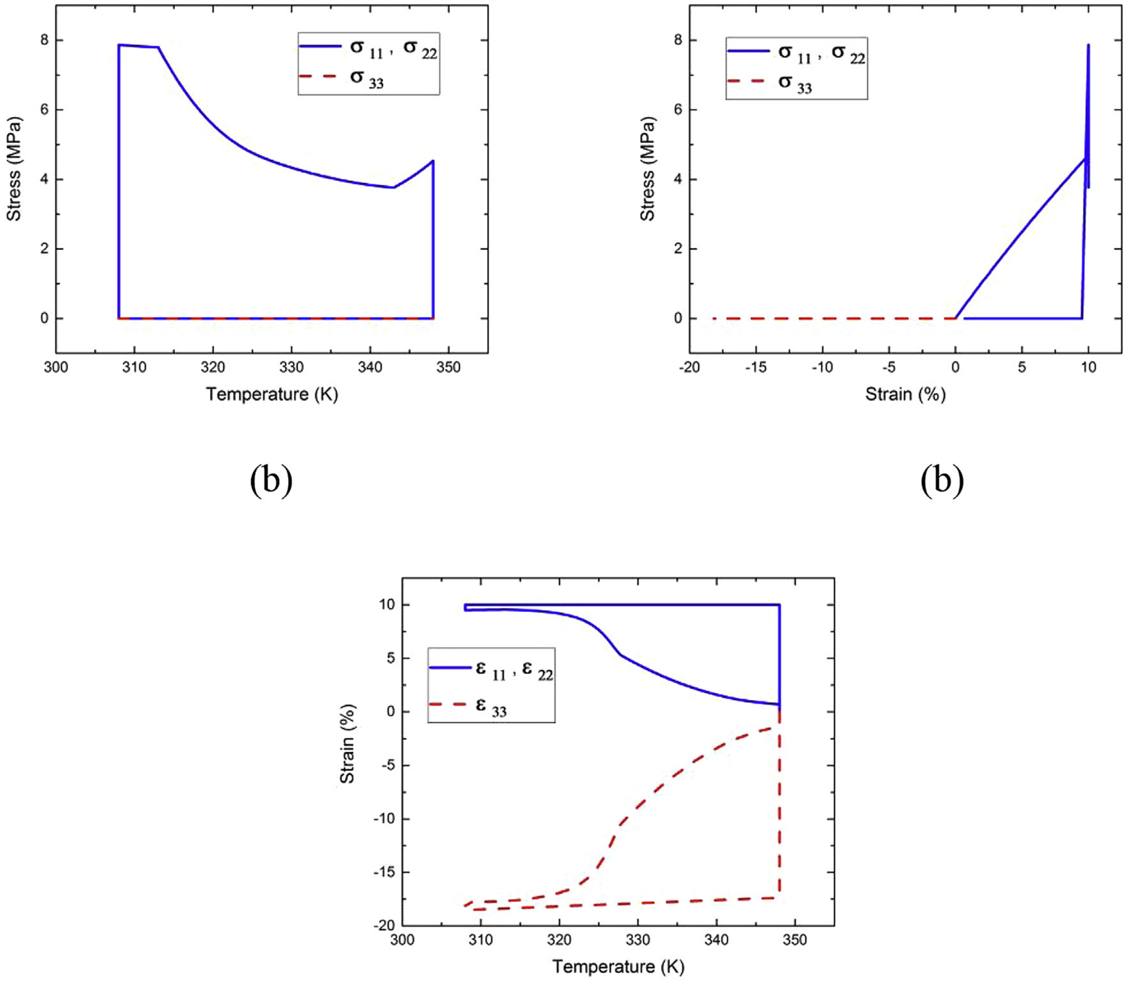

(b)

(b)

(c)

Fig. 8. Simulation of free recovery shape memory cycle for equal-biaxial force case: (a) the stress-temperature curves, (b) stress-strain curves, (c) strain-temperature curves.

(1) In previous research work, there is still a lack of unified constitutive model with shape memory effect. At the same time, most studies of SMPs are only based on a specific material. While our model can be used to various SMPs. The parameters of the model can be easily determined by the corresponding experimental results.

(2) Many models are limited to small strain (within 10%). The current model is also able to simulate the behavior of large strain case.

Acknowledgements

Authors are grateful for the support from the National Natural Science Foundation of China through grant numbers 11372236, 11572236 and 11321062.

References

Ashrafi, M.J., Arghavani, J., Naghdabadi, R., Sohrabpour, S., Auricchio, F., 2016. Theoretical and numerical modeling of dense and porous shape memory alloys accounting for coupling effects of plasticity and transformation. Int. J. Solids Struct. s 88–89, 248–262.

Baghani, M., Arghavani, J., Naghdabadi, R., 2014. A finite deformation constitutive model for shape memory polymers based on hencky strain. Mech. Mater. 73, 1–10.

Baghani, M., Naghdabadi, R., Arghavani, J., Sohrabpour, S., 2012. A thermodynamically-consistent 3D constitutive model for shape memory polymers. Int. J. Plast. 35, 13–30.

Behl, M., Razzaq, M.Y., Lendlein, A., 2010. Multifunctional shape-memory polymers. Adv. Mater 22, 3388–3410.

Bruhns, O.T., Xiao, H., Meyers, A., 2002. Finite bending of a rectangular block of an elastic hencky material. J. Elast. Phys. Sci. Solids 66, 237–256.

Castano, L.M., Flatau, A.B., 2014. Smart fabric sensors and e-textile technologies: a review. Smart Mater. Struct. 23.

Castro, F., Westbrook, K.K., Long, K.N., Shandas, R., Qi, H.J., 2010. Effects of thermal rates on the thermomechanical behaviors of amorphous shape memory polymers. Mech. Time-Depend. Mater. 14, 219–241.

Chen, J., Liu, L., Liu, Y., Leng, J., 2014. Thermoviscoelastic shape memory behavior for epoxy-shape memory polymer. Smart Mater. Struct. 23, 55025–55038 (55014).

Chen, Y.-C., Lagoudas, D.C., 2008a. A constitutive theory for shape memory polymers. Part I. J. Mech. Phys. Solids 56, 1752–1765.

Chen, Y.-C., Lagoudas, D.C., 2008b. A constitutive theory for shape memory polymers. Part II. J. Mech. Phys. Solids 56, 1766–1778.

Chester, S.A., Anand, L., 2010. A coupled theory of fluid permeation and large deformations for elastomeric materials. J. Mech. Phys. Solids 58, 1879–1906.

Chester, S.A., Anand, L., 2011. A thermo-mechanically coupled theory for fluid permeation in elastomeric materials: application to thermally responsive gels. J. Mech. Phys. Solids 59, 1978–2006.

Chester, S.A., Di Leo, C.V., Anand, L., 2015. A finite element implementation of a coupled diffusion-deformation theory for elastomeric gels. Int. J. Solids Struct. 52, 1–18.

Farrokh, B., Khan, A.S., 2010. A strain rate dependent yield criterion for isotropic polymers: low to high rates of loading. Eur. J. Mech.-A/Solids 29, 274–282.

Ge, Q., Luo, X., Rodriguez, E.D., Zhang, X., Mather, P.T., Dunn, M.L., Qi, H.J., 2012. Thermomechanical behavior of shape memory elastomeric composites. J. Mech. Phys. Solids 60, 67–83.

Ghosh, P., Srinivasa, A.R., 2011. A Two-network thermomechanical model of a shape memory polymer. Int. J. Eng. Sci. 49, 823–838.

Ghosh, P., Srinivasa, A.R., 2013. A two-network thermomechanical model and parametric study of the response of shape memory polymers. Mech. Mater. 60, 1–17.

Ghosh, P., Srinivasa, A.R., 2014. Development of a finite strain two-network model for shape memory polymers using QR decomposition. Int. J. Eng. Sci. 81, 177–191.

Gilormini, P., Diani, J., 2012. On modeling shape memory polymers as thermoelastic two-phase composite materials. Comptes Rendus Mécanique 340, 338–348.

Gu, J., Sun, H., Fang, C., 2014. A phenomenological constitutive model for shape memory polyurethanes. J. Intell. Mater. Syst. Struct. 26.

Hager, M.D., Bode, S., Weber, C., Schubert, U.S., 2015. Shape memory polymers: past, present and future developments. Prog. Polym. Sci. 49, 3–33.

He, Y., Guo, S., Liu, Z., Liew, K.M., 2015. Pattern transformation of thermo-responsive shape memory polymer periodic cellular structures. Int. J. Solids Struct. 71, 194–205.

Hencky, H., 1928. Über die form des elastizitätsgesetzes bei ideal elastischen Stoffen. Z. Techn. Phys. 9, 215–220.

Holzapfel, G.A., 2000. Nonlinear solid mechanics : a continuum approach for engineering/G.A. Holzapfel. Meccanica 37, 489–490.

Hu, J., Zhu, Y., Huang, H., Lu, J., 2012. Recent advances in shape–memory polymers: structure, mechanism, functionality, modeling and applications. Prog. Polym. Sci. 37, 1720–1763.

Hu, J.L., Chen, S.J., 2010. A review of actively moving polymers in textile applications. J. Mater. Chem. 20, 3346–3355.

Huang, W.M., Song, C.L., Fu, Y.Q., Wang, C.C., Zhao, Y., Purnawali, H., Lu, H.B., Tang, C., Ding, Z., Zhang, J.L., 2013. Shaping tissue with shape memory materials. Adv. drug Deliv. Rev. 65, 515–535.

Khan, A.S., Baig, M., Hamid, S., Zhang, H., 2010. Thermo-mechanical large deformation responses of hydrogenated nitrile Butadiene rubber (HNBR): experimental results. Int. J. Solids Struct. 47, 2653–2659.

Lee, E., Zhang, M., Cho, Y., Cui, Y., Van, d.S.J., Engheta, N., Yang, S., 2014. Tilted pillars on wrinkled elastomers as a reversibly tunable optical window. Adv. Mater 26, 4127–4133.

Leng, J., Lu, H., Liu, Y., Huang, W.M., Du, S., 2009. Shape-memory polymers—a class of novel smart materials. Mrs Bull. 34, 848–855.

Leng, J., Xin, L., Liu, Y., Du, S., 2011. Shape-memory polymers and their composites: stimulus methods and applications. Prog. Mater. Sci. 56, 1077–1135.

Li, G., Meng, H., Hu, J., 2012. Healable thermoset polymer composite embedded with stimuli-responsive fibres. J. R. Soc. Interface 9, 3279–3287.

Li, G., Shojaei, A., 2012. A viscoplastic theory of shape memory polymer fibres with application to self-healing materials. Proc. R. Soc. A Math. Phys. Eng. Sci. 468, 2319–2346.

Li, Y., Guo, S.-S., He, Y., Liu, Z., 2015. A simplified constitutive model for predicting shape memory polymers deformation behavior. Int. J. Comput. Mater. Sci. Eng. 04, 1550001.

Liu, Y., Gall, K., Dunn, M.L., Greenberg, A.R., Diani, J., 2006. Thermomechanics of shape memory polymers: uniaxial experiments and constitutive modeling. Int. J. Plast. 22, 279–313.

Liu, Z., Toh, W., Ng, T.Y., 2015. Advances in mechanics of soft materials: a review of large deformation behavior of hydrogels. Int. J. Appl. Mech. 735.

Long, K.N., Dunn, M.L., Qi, H.J., 2010. Mechanics of soft active materials with phase evolution. Int. J. Plast. 26, 603–616.

Lu, S., Pister, K., 1975. Decomposition of deformation and representation of the free energy function for isotropic thermoelastic solids. Int. J. Solids Struct. 11, 927–934.

Marshall, J.E., Gallagher, S., Terentjev, E.M., Smoukov, S.K., 2014. Anisotropic colloidal micromuscles from liquid crystal elastomers. J. Am. Chem. Soc. 136, 474–479.

McClung, A.J., Tandon, G.P., Baur, J.W., 2013. Deformation rate-, hold time-, and cycle-dependent shape-memory performance of Veriflex-E resin. Mech. Time-Depend. Mater. 17, 39–52.

Moon, S., Cui, F., Rao, I.J., 2015. Constitutive modeling of the mechanics associated with triple shape memory polymers. Int. J. Eng. Sci. 96, 86–110.

Mooney, M., 1940. A theory of large elastic deformation. J. Appl. Phys. 11, 582–592.

Nguyen, T.D., Qi, H.J., Castro, F., Long, K.N., 2008. A thermoviscoelastic model for amorphous shape memory polymers: incorporating structural and stress relaxation. J. Mech. Phys. Solids 56, 2792–2814.

Ohm, C., Brehmer, M., Zentel, R., 2010. Liquid crystalline elastomers as actuators and sensors. Adv. Mater 22, 3366–3387.

Oliveira, S.A., Savi, M.A., Santos, I.F., 2014. Uncertainty analysis of a one-dimensional constitutive model for shape memory alloy thermomechanical description. Int. J. Appl. Mech. 6, 1450067.

Onaka, S., 2010. Equivalent strain in simple shear deformation described by using the hencky strain. Philos. Mag. Lett. 90, 633–639.

Poorasadion, S., Arghavani, J., Naghdabadi, R., Sohrabpour, S., 2015. Implementation of microplane model into three-dimensional beam element for shape memory alloys. Int. J. Appl. Mech. 7.

Qi, H.J., Nguyen, T.D., Castro, F., Yakacki, C.M., Shandas, R., 2008. Finite deformation thermo-mechanical behavior of thermally induced shape memory polymers. J. Mech. Phys. Solids 56, 1730–1751.

Rajagopal, K., Srinivasa, A., 1998a. Mechanics of the inelastic behavior of materials—Part 1, theoretical underpinnings. Int. J. Plast. 14, 945–967.

Rajagopal, K., Srinivasa, A., 1998b. Mechanics of the inelastic behavior of materials. Part II: inelastic response. Int. J. Plast. 14, 969–995.

Ratna, D., Karger-Kocsis, J., 2008. Recent advances in shape memory polymers and composites: a review. J. Mater. Sci. 43, 254–269.

Reese, S., Böl, M., Christ, D., 2010. Finite element-based multi-phase modelling of shape memory polymer stents. Comput. Methods Appl. Mech. Eng. 199, 1276–1286.

Reese, S., Govindjee, S., 1998. A theory of finite viscoelasticity and numerical aspects. Int. J. solids Struct. 35, 3455–3482.

Rivlin, R.S., 1948. Large elastic deformations of isotropic materials. IV. further developments of the general theory. Philosophical Trans. R. Soc. A Math. Phys. Eng. Sci. 241, 379–397.

Shojaei, A., Li, G., 2014. Thermomechanical constitutive modelling of shape memory polymer including continuum functional and mechanical damage effects. Proc. R. Soc. A Math. Phys. Eng. Sci. 470.

Srivastava, V., Chester, S.A., Anand, L., 2010. Thermally actuated shape-memory polymers: experiments, theory, and numerical simulations. J. Mech. Phys. Solids 58, 1100–1124.

Sweeney, J., Shirataki, H., Unwin, A.P., Ward, I.M., 1999. Application of a necking criterion to PET fibers in tension. J. Appl. Polym. Sci. 74, 3331–3341.

Tobushi, H., Hashimoto, T., Hayashi, S., Yamada, E., 1997. Thermomechanical constitutive modeling in shape memory polymer of polyurethane series. J. Intelligent Material Syst. Struct. 8, 711–718.

Tobushi, H., Okumura, K., Hayashi, S., Ito, N., 2001. Thermomechanical constitutive model of shape memory polymer. Mech. Mater. 33, 545–554.

Volk, B.L., Lagoudas, D.C., Chen, Y.C., 2010. Analysis of the finite deformation response of shape memory polymers: II. 1D calibration and numerical implementation of a finite deformation, thermoelastic model. Smart Mater. Struct. 19, 1–4.

Voyiadjis, G.Z., Amir, S., Guoqiang, L.I., 2011a. A thermodynamic consistent damage and healing model for self healing materials. Int. J. Plast. 27, 1025–1044.

Voyiadjis, G.Z., Shojaei, A., Li, G., Kattan, P.I., 2011b. A theory of anisotropic healing and damage mechanics of materials. Proc. R. Soc. Lond. A Math. Phys. Eng. Sci. R. Soc. 468, 163–183 rspa20110326.

Wong, Y.S., Stachurski, Z.H., Venkatraman, S.S., 2011. Modeling shape memory effect in uncrosslinked amorphous biodegradable polymer. Polymer 52, 874–880.

Xu, H., Yu, C., Wang, S., Malyarchuk, V., Xie, T., Rogers, J.A., 2013. Shape-memory polymers: deformable, programmable, and shape-memorizing micro-optics (adv. Funct. Mater. 26/2013). Adv. Funct. Mater. 23, 3299–3306.

Xu, W., Li, G., 2010. Constitutive modeling of shape memory polymer based self-healing syntactic foam. Int. J. Solids Struct. 47, 1306–1316.

Yang, Q., Li, G., 2015. Temperature and rate dependent thermomechanical modeling of shape memory polymers with physics based phase evolution law. Int. J. Plast. 80, 168–186.

Yu, C., Kang, G., Kan, Q., 2014. Crystal plasticity based constitutive model of NiTi shape memory alloy considering different mechanisms of inelastic deformation. Int. J. Plast. 54, 132–162.